

## Corotating Dust Clumps Around Adolescent Low-Mass Stars: Four Years of TESS

LUKE G. BOUMA,<sup>1,\*</sup> RAHUL JAYARAMAN,<sup>2</sup> SAUL RAPPAPORT,<sup>2</sup> LYNNE A. HILLENBRAND,<sup>1</sup> AND GEORGE R. RICKER<sup>2</sup>

<sup>1</sup>*Department of Astronomy, MC 249-17, California Institute of Technology, Pasadena, CA 91125, USA*

<sup>2</sup>*MIT Kavli Institute and Department of Physics, 77 Massachusetts Avenue, Cambridge, MA 02139*

(Received —; Revised —; Accepted —)

### ABSTRACT

Complex quasiperiodic variables (CQVs) are low-mass pre-main-sequence stars with nearly periodic optical modulation. The modulation is likely induced by dust or gas clumps in orbit at the Keplerian corotation radius. Here, we report new CQVs discovered in TESS data collected between July 2018 and Sep 2022. Our search of 65760 K- and M-dwarfs with  $T < 16$  and  $d < 150$  pc yielded 53 gold-standard CQVs. Most of these discoveries are new, and they include the brightest and closest examples of this class of object known ( $T \approx 9.5$ ;  $d \approx 20$  pc), as well as the most massive ( $\approx 0.65 M_{\odot}$ ). A few objects are outliers among outliers; LP 12-502 for instance shows a “dip complex” with a period and total duration that are fixed over more than 1,000 cycles, but which in detail shows anywhere from four to eight local minima per cycle. LP-502 at times demonstrated drastic shape changes over less than one cycle, and also displayed distinct superposed periods simultaneously. Broadly speaking, we find that none of the CQVs maintain a fixed light curve shape over timescales of more than a few hundred cycles, and we revisit the arguments for why transient corotating material is the most likely explanation. In the future, we expect that our sample will facilitate modeling and observational efforts aimed at understanding these objects, and connecting them to the broader contexts of star, disk, and exoplanet evolution.

**Keywords:** Weak-line T Tauri stars (1795), Periodic variable stars (1213), Circumstellar matter (241), Star clusters (1567), Stellar magnetic fields (1610), Stellar rotation (1629)

### 1. INTRODUCTION

All pre-main-sequence stars vary in optical brightness, and the origin of such variability is, in most cases, understood. Well-explored sources of optical variability include inhomogeneities on stellar surfaces such as starspots and faculae (Basri 2021), occultations by gas-rich circumstellar disks (Bodman et al. 2017), and, in geometrically favorable circumstances, eclipses by stars and planets (Winn 2010). More exotic forms of optical variability relevant to this work include transiting exocomets (e.g.  $\beta$  Pic; Zieba et al. 2019) and disintegrating rocky bodies around both M-dwarfs (e.g. K2-22; Rappaport et al. 2014) and white dwarfs (e.g. WD 1145; Vanderburg et al. 2015).

Data from K2 and TESS have yielded a new class of variable star whose root cause is only beginning to become clear: complex quasiperiodic variables (CQVs). These objects are identified phenomenologically using their optical light curves, which show nearly periodic troughs that can be either sharp or broad, often superposed on smooth spot-like modulation (Stauffer et al. 2017, 2018; Zhan et al. 2019).

Some CQVs show up to eight local minima (dips) per cycle. Most CQVs are pre-main-sequence M-dwarfs without near-infrared excesses, with ages of  $\approx 5$ -150 million years (Myr), and rotation periods of at most two days; they are observed to be  $\approx 1$ -3% of M-dwarfs younger than 100 Myr (Rebull et al. 2016; Günther et al. 2022). The dips can be chromatic, with a reddening law plausibly consistent with dust (Bouma et al. 2020; Günther et al. 2022; Koen 2023). And finally, while the dip shapes can “jump” between different depths and durations over less than one cycle, they more often evolve gradually, over tens to hundreds of cycles (e.g. Stauffer et al. 2017; Palumbo et al. 2022; Popinchalk et al. 2023).

A few competing explanations for what causes the complex quasiperiodic variability are shown in Figure 1, along with a few representative light curves. All young M-dwarfs are spotted, which produces flux variations over characteristic timescales of the rotation period,  $P_{\text{rot}}$ , and its half-harmonic,  $0.5P_{\text{rot}}$ . The observed dips occur over durations as short as  $0.05P_{\text{rot}}$ ; a “starspot-only” scenario can be discarded for any object with sufficiently sharp dips (Stauffer et al. 2017; Koen 2021). The more likely scenarios invoke sharp geometries with material extrinsic to the stellar surface (e.g. Stauffer et al. 2017; Günther et al. 2022). In the “clump” scenario, opaque dust clumps orbiting near the Keplerian corotation radius eclipse the star (Stauffer et al. 2017;

Corresponding author: Luke G. Bouma  
luke@astro.caltech.edu

\* 51 Pegasi b Fellow

(Sanderson et al. 2023). In the “prominence” scenario, long-lived condensations of plasma are trapped along the star’s magnetic field lines, also near corotation (Waugh & Jardine 2022). There is also a “screen” scenario, in which the inner wall of a quiescent circumstellar disk blocks a portion of the stellar surface to produce sudden dips whenever spots come into view (Zhan et al. 2019).

In our view, the arguments seem best established for the dust clump hypothesis (Sanderson et al. 2023). This is primarily because the prominence scenario lacks a mechanism for generating broadband opacity, and the screen scenario is inconsistent with the degree of observed periodicity, the lack of infrared excess, and the observed lifetime of the effect, which is an order of magnitude longer than the  $\approx 10^7$  year timescale typically quoted for the primordial disk to disperse. However, unambiguous evidence, for instance a spectroscopic detection of silicates during a “dip”, has yet to be acquired.

CQVs have been challenging to understand because they have been both hard to discover and hard to characterize. Discoverability is tied to rarity: CQVs comprise about 1% of the youngest 1% of M-dwarfs (Rebull et al. 2018). Out of the millions of stars monitored by K2 and TESS, about 50 CQVs have been reported to date (Rebull et al. 2016; Stauffer et al. 2017, 2018; Zhan et al. 2019; Bouma et al. 2020; Günther et al. 2022; Popinchalk et al. 2023). The known CQVs are correspondingly faint; the initial K2 discoveries (Rebull et al. 2016; Stauffer et al. 2017) were M2-M6 dwarfs at distances  $\gtrsim 100$  pc, yielding optical brightnesses of  $V \approx 15.5$  to  $V > 20$ . This renders time-series spectroscopy at high resolution technically impossible, despite its potential utility in ruling between the models.

One way to help rule between the mechanisms is to therefore find bright and nearby CQVs, since these objects will be the most amenable to detailed photometric and spectroscopic analyses. To do this, in this work, we use 120-second cadence data acquired by TESS between July 2018 and Sep 2022 (Sectors 1-55; Cycles 1-4). We present our search methods in Section 2; and the properties of the resulting CQV catalog in Section 3. Open questions are discussed in Section 5, and we conclude in Section 6.

A word on nomenclature. CQVs have been called “transient and persistent flux dips”, “scallop shells”, “batwings”, (Stauffer et al. 2017) “complex rotators”, (Zhan et al. 2019; Günther et al. 2022; Popinchalk et al. 2023) and “complex periodic variables” (Koen 2023). The CQVs should not be conflated with “dippers”, which are classical T Tauri stars with infrared excesses whose optical variability is linked to obscuring inner disk structures and accretion hot spots (Cody et al. 2014; Robinson et al. 2021). At the risk of introducing yet another standard, we prefer a nomenclature that reflects how, when observed over timescales of more than tens of cycles, CQVs are almost, but not exactly periodic. Their shape evolution implies that they are irregularly periodic, or for short, quasiperiodic. While the three-type classification scheme proposed by Stauffer et al. (2017) may indeed provide some helpful visual distinctions amongst CQV sub-

classes, it seems likely that they are all explained by a single underlying phenomenon, and so we opt to refer to them by a single empirically descriptive name.

## 2. METHODS

### 2.1. Stellar selection function

We analyzed the “short” 120-second cadence data acquired by TESS between July 2018 and Sep 2022 (Sectors 1-55). Specifically, we used the 120-second cadence light curve products produced by the mission’s Science Processing and Operations Center at NASA Ames (Jenkins et al. 2016). While the TESS data products also include full frame images with cadences of 200, 600, and 1800 seconds, we limited our scope in this work for the sake of simplicity in data handling. In exchange, we lose in both completeness and homogeneity of the selection function. While TESS cumulatively observed  $\approx 90\%$  of the sky for at least one lunar month between July 2018 and Sep 2022, the 120-second cadence data were acquired for only a pre-selected set of stars over Sectors 1-26, and then a guest-investigator driven set of stars over Sectors 27-55 (Fausnaugh et al. 2021).

To assess the completeness of the resulting 120-second cadence data that is the basis of this study, we cross-matched TIC8 (Stassun et al. 2018) against the Gaia DR2 point-source catalog (Gaia Collaboration et al. 2018). We opted for Gaia DR2 rather than DR3 because the base catalog for TIC8 was Gaia DR2, which facilitated a one-to-one crossmatch using the Gaia source identifiers. This exercise showed that for  $T < 16$  M-dwarfs, the TESS 2-minute data are roughly 50% complete at  $\approx 50$  pc. At  $< 20$  pc,  $\gtrsim 80\%$  of the  $T < 16$  M-dwarfs have at least one sector of short-cadence data; at  $> 100$  pc,  $\lesssim 10\%$  of such M-dwarfs have at least one sector of short-cadence data. Armed with this understanding, we then used our cross-match between Gaia DR2 and TIC8 to select our stars of interest, which we defined as stars with 120-second cadence TESS light curves that satisfied

$$T < 16 \quad (\text{Bright for TESS}) \quad (1)$$

$$G_{\text{BP}} - G_{\text{RP}} > 1.5 \quad (\text{Red stars only}) \quad (2)$$

$$M_G > 4 \quad (\text{Dwarf stars only}) \quad (3)$$

$$d < 150 \text{ pc} \quad (\text{Close stars only}), \quad (4)$$

for  $M_G = G + 5 \log(\varpi_{\text{as}}) + 5$  the Gaia  $G$ -band absolute magnitude,  $\varpi_{\text{as}}$  the parallax in units of arcseconds, and a geometric distance  $d$  defined by inverting the parallax and ignoring any zero-point correction. This selection function includes dwarf stars later than spectral types of  $\approx \text{K}6\text{V}$  (Pecaut & Mamajek 2013). The target sample therefore includes 65760 M-dwarfs and late-K dwarfs, down to  $T < 16$  and out to  $d < 150$  pc.

### 2.2. CQV discovery

Previous methods for finding CQVs have included visually examining stars known to be in young clusters (Rebull et al. 2016; Stauffer et al. 2017), and automatically flagging rapid rotators with a large number of strong Fourier harmonics (Zhan et al. 2019). The latter approach still requires visual



**Figure 1. Complex quasiperiodic variables (CQVs):** *Top:* Phase-folded TESS light curves of three CQVs. Each is stacked over one month. Gray are raw 2-minute data; black bins to 300 points per cycle. Periods in hours are in the bottom right of each panel. In order left-to-right, the objects are LP 12-502 (TIC 402980664; Sector 19), TIC 94088626 (Sector 10), and TIC 425933644 (Sector 28). *Bottom:* Plausible cartoon models for the phenomenon. The dust clump scenario seems most plausible, given the stability of the dips, their chromaticity, the lack of observed infrared excesses, and the challenge of producing broadband opacity variations with only ionized hydrogen in the prominence scenario.

vetting, since “stars with many Fourier harmonics” is a designation that includes objects such as eclipsing binaries or multiple stars blended into a single photometric aperture. In this work, we implemented a new search approach based on counting the number of sharp local minima in phase-folded light curves, while also using the previously tested Fourier approach. We applied these two search techniques independently.

### 2.2.1. Counting dips

The dip counting technique aims to count sharp local minima in phase-folded light curves. CQVs will preferably have at least three such minima in order to be distinct from false positives such as synchronized and spotted binaries (“RS CVn” stars).

For our dip-counting pipeline, we began with the PDC\_SAP flux for each sector, removed non-zero quality flags, and normalized the light curve to one by dividing out its median value. We then flattened the light curve using a 5-day sliding median filter, as implemented in `wotan` (Hippke et al. 2019). On the resulting cleaned and flattened light curve, we ran a periodogram search, opting for the Stellingwerf (1978) phase dispersion minimization (PDM) algorithm implemented in `astrobase` (Bhatti et al. 2021) due to its shape agnosticism. If a period below 2 days was identified, we reran the periodogram at a finer grid to improve the accuracy of the period determination.

Once a star’s period  $P$  was identified, we binned the phased light curve to 100 points per cycle. To separate “sharp” local minima from smooth spot-induced variability, we then

iteratively fit penalized splines to the wrapped phase-folded light curve, excluding points more than two standard deviations away from the local continuum (Hippke et al. 2019). The maximum number of equidistant spline knots per cycle is the parameter in this framework that controlled the meaning of “sharp”—we allowed at most 10 such knots per cycle, though for most stars fewer knots were preferred based on an  $\ell^2$ -norm penalty.

We then identified local minima in the resulting residual light curve using the SciPy `find_peaks` utility (Virtanen et al. 2020), which is based on comparing adjacent values in an array. For a peak to be flagged as significant, we required it to have a width of at least  $0.02P$ , and a height of at least twice the point-to-point RMS. This latter quantity is defined as the 68<sup>th</sup> percentile of the distribution of the residuals from the median value of  $\delta f_i \equiv f_i - f_{i+1}$ , where  $f$  is the flux and  $i$  is an index over time.

To correctly identify local minima near the edges of the phased light curve, which usually would cover phases  $\phi \in [0, 1]$ , we in fact performed the entire procedure over a phase-folded light curve spanning  $\phi \in [-1, 2]$ , by duplicating and concatenating the ordinary phase-folded light curve. The free parameters we adopted throughout this analysis procedure, for instance the maximum number of spline knots per cycle, and how large and wide of a local minimum to consider a “true dip”, were chosen during a testing period based on their ability to correctly re-identify a large fraction ( $>90\%$ ) of known CQVs, while also being able to consistently reject common false positives such as rapidly rotating spot-induced variability and typical eclipsing binaries.

Overall, for a star to clear this process and to proceed to manual examination, we required that it have a peak PDM period below two days, and that it exhibited at least three sharp local minima (as algorithmically reported) in at least one observed TESS sector.

### 2.2.2. Fourier analysis

For the Fourier analysis, we followed Zhan et al. (2019).

**TODO for Rahul or Saul: explain the approach, in a few paragraphs. Was the SAP\_FLUX or PDCSAP used? etc.**

### 2.2.3. Manual vetting

We visually assessed whether the objects found using the Fourier (Section 2.2.2) and dip-counting (Section 2.2.1) techniques were consistent with expectations for CQVs by assembling the data shown in Appendix A. We labelled a star as a “good” CQV if at least one TESS sector showed what we viewed as the unambiguous signatures of the class (short period; at least three dips or else otherwise oddly-shaped dips; relative stability over a timescale of 30 days). We also noted stars that we thought could be CQVs, but that were more ambiguous with a “maybe” flag.

Broadly speaking, the most common false positives for both the Fourier and dip-counting techniques were eclipsing binaries, spot-induced variability from rapid rotators, and variability from neighboring, off-target stars. Typical false positive rates from our dip-counting pipeline were 5:1, with 368 unique stars flagged, and about 20% being labelled either “good” or “possible” CQVs; for the Fourier pipeline, the rate was X:Y, with ZZZZ unique stars flagged, and NN% being labelled “good” or “possible” CQVs.

## 2.3. Stellar properties

**Ages**—We estimated the stellar ages by making probabilistic spatial and kinematic associations between the CQVs and known clusters in the solar neighborhood. For most stars in our sample, we did this using BANYAN  $\Sigma$  (Gagné et al. 2018).<sup>1</sup> This algorithm calculates the probability that a given star belongs to one of 27 young clusters (or “associations”) within 150 pc of the Sun, by modeling the clusters as multivariate Gaussians in 3-D position and 3-D velocity space. We used the Gaia DR2 sky positions, proper motions, and distances to calculate the membership probabilities. BANYAN  $\Sigma$  in turn analytically marginalizes over the radial velocity dimension. The probabilities returned by this procedure are qualitatively useful, but we emphasize that they are quantitatively dubious due to the non-Gaussian nature of most groups within the solar neighborhood (see e.g. Kerr et al. 2021, Figure 10).

For a few cases where BANYAN  $\Sigma$  yielded ambiguous results, we consulted the meta-catalog of young, age-dated, and age-dateable stars within a kiloparsec from Bouma et al.

(2022), and also searched the local volume around each star for co-moving companions.<sup>2</sup>

*Effective temperatures, radii, and masses*—We determined the stellar effective temperature and radii through SED fitting; we then estimated the masses by interpolating against the PARSEC v1.2S models (Bressan et al. 2012; Chen et al. 2014).

For the SED fitting, we used astroARIADNE (Vines & Jenkins 2022). We adopted the “BT-Settl” stellar atmosphere models (Allard et al. 2012) assuming the Asplund et al. (2009) solar abundances, and the Barber et al. (2006) water line lists. The broadband magnitudes we considered included  $GG_{\text{BP}}G_{\text{RP}}$  from Gaia DR2,  $Vgri$  from APASS,  $JHK_S$  from 2MASS, SDSS  $r_{iz}$ , and the WISE 1-2 passbands. We specifically omitted UV flux measurements to avoid biasing our fit with any possible chromospheric UV excess. astroARIADNE compares the measured broadband flux measurements against pre-computed model grids, and by default fits for six parameters:  $\{T_{\text{eff}}, R_{\star}, A_V, \log g, [\text{Fe}/\text{H}], d\}$ . The distance prior is drawn from Bailer-Jones et al. (2021). The surface gravity and metallicity are generally unconstrained. And finally, given our particular use-case, we assumed the following priors for the temperature, stellar size, and extinction:

$$T_{\text{eff}}/\text{K} \sim \mathcal{N}(3000, 1000), \quad (5)$$

$$R_{\star}/R_{\odot} \sim \mathcal{T}_N(0.5, 0.3, 0.1, 1.5), \quad (6)$$

$$A_V/\text{mag} \sim \mathcal{U}(0, 0.2), \quad (7)$$

for  $\mathcal{N}$  the Gaussian and  $\mathcal{U}$  the uniform distributions, and  $\mathcal{T}(\mu, \sigma, a, b)$  a truncated normal distribution with mean  $\mu$ , standard deviation  $\sigma$ , and lower and upper bounds  $a$  and  $b$ . Using Dynesty (Speagle 2020), we statically sampled the posterior probability assuming the default Gaussian likelihood, and set a stopping threshold of  $d\log \mathcal{Z} < 0.01$ , where  $\mathcal{Z}$  denotes the evidence.

With the effective temperatures and stellar radii from the SED fit, we then estimated the stellar masses by interpolating against the PARSEC isochrones (v1.2S Chen et al. 2014). The need for models that incorporate some form of correction for young, active M-dwarfs is well-documented (e.g. Stassun et al. 2012; David & Hillenbrand 2015; Feiden 2016; Somers et al. 2020). Plausible explanations for anomalous M-dwarf colors and sizes relative to model predictions include star starspot coverage (e.g. Gully-Santiago et al. 2017), and potentially incomplete line lists (e.g. Rajpurohit et al. 2013). In the PARSEC models, Chen et al. (2014) performed an empirical correction to the temperature–opacity relation drawn from the BT-Settl model atmospheres, in order to match observed masses and radii of young eclipsing binaries. This is sufficient for our purpose of estimating accurate stellar masses. Given our observed  $\{\tilde{T}_{\text{eff}}, \tilde{M}_{\star}, \tilde{r}\}$ , and approximating their uncertainties as Gaussian  $\sigma_{\tilde{T}_{\text{eff}}}$ ,  $\sigma_{\tilde{M}_{\star}}$  and  $\sigma_{\tilde{r}}$ , we evaluate a

<sup>1</sup> [https://github.com/jgagneastro/banyan\\_sigma](https://github.com/jgagneastro/banyan_sigma), git commit 394b486

<sup>2</sup> <https://github.com/adamkraus/Comove>, git commit 278b372

distance  $d$  between our observations and any model PARSEC grid-point  $\{T_{\text{eff}}, M_*, t\}$  as

$$d^2 = \left( \frac{\tilde{T}_{\text{eff}} - T_{\text{eff}}}{\sigma_{\tilde{T}_{\text{eff}}}} \right)^2 + \left( \frac{\tilde{M}_* - M_*}{\sigma_{\tilde{M}_*}} \right)^2 + \left( \frac{\tilde{t} - t}{\sigma_{\tilde{t}}} \right)^2, \quad (8)$$

in order to assign equal importance to each dimension. The preferred model mass is then one that minimizes this distance, and is quoted in Table ??.

### 3. RESULTS

#### 3.1. CQV catalog

Table ?? lists the 70 CQVs identified by our search, along important physical and observational properties. 53 objects demonstrated what we viewed as unambiguous characteristics of the CQV phenomenon in at least one TESS sector; we refer to these as the “gold sample”. We found the remaining 17 CQV candidates to be ambiguous; their variability might be caused by say, multiple starspot groups. Additional data from TESS or other instruments could help resolve their classification. In the following discussion, we will primarily restrict our discussion to the gold sample.

The mosaic in Figure 2 shows phased light curves for the 53 bona fide CQVs. The objects are sorted first in order of the number of TESS 120-second cadence sectors in which they clearly demonstrated the CQV phenomenon, and secondarily by descending brightness. The objects at the top generally have the most 120-second cadence data. The top five objects by this metric are TIC 300651846 ( $T=13.5$ , 12 sectors); TIC 402980664 ( $T=11.1$ , 7 sectors); TIC 89463560 ( $T=13.5$ , 5 sectors); TIC 363963079 ( $T=12.9$ , 5 sectors); and TIC 294328887 ( $T=14.2$ , 4 sectors). The brightest five CQVs span  $9.3 < T < 11.1$ ; the faintest five span  $14.5 < T < 15.0$ . The fastest five have periods spanning 3.6 hr  $< P <$  6.2 hr, while the slowest five span 27 hr  $< P <$  38 hr.

In terms of the light curve shapes, Figure 2 shows a broad range of variability, with anywhere from two to eight local minima per cycle. Some stars show relatively ordinary modulation during one continuous portion of the phased light curve, and highly structured modulation in the remainder of the cycle (e.g. TIC 206544316, TIC 224283342, TIC 402980664). Others show structured modulation over the entire span of a cycle (e.g. TIC 2234692, TIC 401789285, TIC 425933644, TIC 142173958). Others still show some mix between these two modes.

A small number of objects at first glance seem reminiscent of eclipsing binaries, such as TIC 193831684 or TIC 5714469. In these few cases, we believe that that are unlikely to be eclipsing binaries due to additional coherent variations in the light curves that are distinct from any binary phenomenology of which we are aware.

#### 3.2. Ages

Of our 70 confirmed and candidate CQVs, 67 were associated with a nearby moving group or open cluster using BANYAN  $\Sigma$ . The relevant groups are listed in Table ??; their

ages span  $\approx$ 5-150 Myr. The most prodigious groups were Sco-Cen, Tuc-Hor, and Columba. The yield in Sco-Cen is not particularly surprising, since Sco-Cen contains the majority of pre-main-sequence stars in the solar neighborhood. However it is certainly likely given the  $\lesssim$ 10% completeness of TESS beyond 100 pc that far more CQVs remains to be discovered in Sco-Cen. IC 2602 and IC 2391, which are located slightly beyond 100 pc, are an example of this completeness effect: no CQVs appear in those clusters from our search.

Of the three stars for which BANYAN  $\Sigma$  did not find any association, one (TIC 302160226) is a member of  $\alpha$  Per ( $t \approx 86 \pm 16$  Myr; Meingast et al. 2021; Boyle & Bouma 2023). For the other two (TIC 58084670 and TIC 141146667), we were not able to confidently associate either star with any young groups. However both do seem to clearly show the CQV signal over multiple TESS sectors, and both are photometrically elevated relative to the main sequence. For instance, both were noted as being in the “diffuse” Class III YSO population near the Sun by Kerr et al. (2021).

Our catalog confirms that the CQV phenomenon persists for at least  $\approx$ 150 Myr. Our catalog includes three  $\approx$ 150 Myr CQVs in AB Dor (Bell et al. 2015): TIC 288344202, TIC 332517282, and TIC 368129164. There is also a  $\approx$ 112 Myr old Pleiades CQV (TIC 440725886; Dahm 2015; Cantat-Gaudin et al. 2020), and a similarly-aged Psc-Eri member (TIC 38539720; Ratzenböck et al. 2020). To our best knowledge, TIC 332517282 was the previous record-holder for oldest-known CQV (Zhan et al. 2019; Günther et al. 2022); at least one unambiguous case (EPIC 211070495) and a few other candidates were also previously known in the Pleiades (Rebull et al. 2016). While we expect to have been sensitive to CQVs in the nearby Hyades ( $\approx$ 700 Myr), again due to the specifics of the TESS 120-second selection function, we do not know at this time whether we would have been sensitive to such stars.

Finally, six CQVs were identified in the recently confirmed Argus association (Zuckerman 2019). This serves as an indirect line of evidence supporting the reality, and youth, of that group.

#### 3.3. Infrared excesses

As is typical for CQVs (Stauffer et al. 2017), most CQVs in our catalog did not show infrared excesses in the WISE1-4 bands. Visually inspecting the SEDs of our entire 70 star sample, we labelled two objects as having “good” infrared excesses (both W3 and W4), and three as “possible” infrared excess.

The two “good” IR excesses belonged to “candidate” CQVs TIC 193136669 (TWA 34) and TIC 57830249 (TWA 33). Both are in the TW Hydrae association ( $\approx$ 10 Myr), and have relatively long periods of 38 hr and 44 hr respectively. In our initial labelling, we labelled both as “maybe” CQVs because the dips in their light curves did not show the rigid periodicity typical of CQVs; their periods were also relatively long. After labelling them, inspection of further sectors clarified that both sources are dippers (see

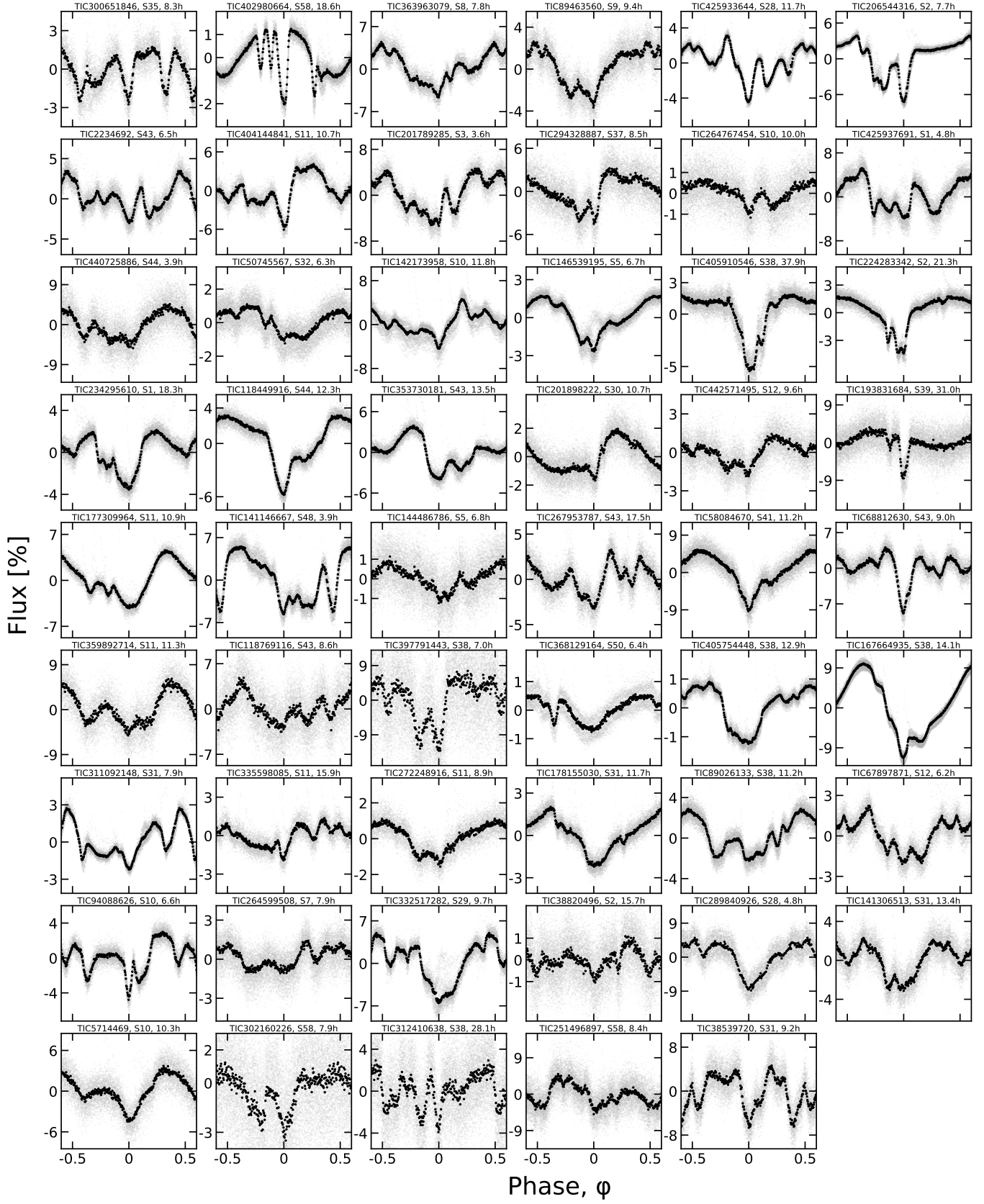


**Figure 2. CQVs found in the TESS 2-minute data.** Phased TESS light curves over one month are shown for 53 CQVs. Gray are raw 2-minute data; black bins to 300 points per cycle. Each panel is labelled by the TIC identifier, the TESS sector number, and the period in hours. Objects are ordered such that sources with the most TESS data available are on top (see Section 3.1).

plots in Appendix A). In addition, TIC 193136669 has a cold molecular disk based on observed 1.3 mm continuum emission and resolved Keplerian  $^{12}\text{CO}(2-1)$  emission (Rodriguez et al. 2015). It was also labelled a dipper by Capistrant et al. (2022); we agree with their designation, but nonetheless leave it in our catalog as an indication of possible ambiguities in our search process. TIC 57830249 (TWA 33) also has previously detected 1.3 mm continuum emission (Rodriguez et al. 2015), suggestive of cold dust grains being present. It therefore also a dipper that snuck its way into our “maybe” pile.

Our three “possible” infrared excesses were TIC 405910546, 289840926, and 244161191. After a literature search, we concluded that none have clear evidence for the presence of a disk. TIC 405910546, in LCC, shows a unique TESS light curve, reminiscent of a  $P=38$  hr singly-eclipsing binary, except with additional substructure during each eclipse that resembles the CQV phenomenon more than any other variability of which we are aware. TIC 289840926 ( $\beta$  Pic moving group,  $P=4.8$  hr), show what we believe is a clear CQV signals, but has no definitive evidence for a large, dusty disk. TIC 244161191 (hilariously, TOI-278), in Columba, also has no definitive evidence for a large disk. It is however “multi-periodic”—in addition to the 7.17 hr CPV signal, this source shows a superposed 8.39 hr sinusoidal signal, probably from an unresolved neighboring star.

Comparing these results against the backdrop of our increasing understanding of dippers (e.g. Cody et al. 2014; Ansdell et al. 2016; Robinson et al. 2021; Capistrant et al. 2022), it is clear that the loss of an infrared excess is associated with strong changes in a star’s optical variability. It is reasonable to imagine connections between CQVs and dippers: both classes of object can show transient flux dips that are relatively narrow in duration. Such dips are probably caused by clumps of dust. However the CQV dips are typically *i*) more periodic and *ii*) less deep than those of dippers, and *iii*) they display far less transience over timescales of a few to tens of cycles. This is probably because CQV stars have demonstrably less dust than dipper stars. At a population level, the CQV stars are also older. A common mystery between the CQVs and dippers, in our own estimation, is how exactly the *narrowness* of the dust clumps is produced. It is not unreasonable to imagine a similar mechanism operating for both types of object, tied perhaps to a shared magnetic topology, or perhaps to a preference for dust to inspiral to the star in clumped structures.

## 4. CQV EVOLUTION

### 4.1. Evolution over two year baseline

Figure 3 shows “before” and “after” views of 27 CQVs for which TESS 120-second cadence observations were available at least two years apart. Such a baseline was available for 32 of the confirmed 53 CQVs in our catalog; for plotting purposes we show the brightest 27. Of these 27 CQVs, a few show clear signs of the phenomenon in one sector, and marginal or non-existence signs in the other. While there is some subjectivity in this assessment, to our

eyes cases for which at least one sector would be flagged as “ambiguous” include TIC 368129164 (Sector 23 might be labelled an EB), TIC 177309964 (Sector 38 would be simply a rotating star), TIC 404144841 (Sector 38 looks like a rotating star), TIC 201898222 (Sector 3 looks like a rotating star), TIC 144486786 (Sector 32 might be an RS CVn), and TIC 38820496 (Sector 28 might be an RS CVn). TIC 193831684, assessed on a single-sector basis, would probably be labelled an eclipsing binary—in fact, Justesen & Albrecht (2021) implicitly have already given this source such a label! Based on the shape evolution between Sectors 13 and 39 however, it is a CQV. One could easily also imagine in cases like TIC 206544316 that if observed at lower signal to noise, the drastic shape evolution would not be appreciated. We emphasize that the periods themselves were all stable to  $<0.1\%$ . Broadly speaking, this shape evolution suggests that CQVs have an “on/off” duty cycle of  $\approx 75\%$ . This type of correction is likely worth including in population-level estimates of how intrinsically common CQVs are in the low-mass stellar population (e.g. Günther et al. 2022).

### 4.2. Evolution over adjacent sectors, & LP 12-502

#### 4.2.1. LP 12-502 observations

While many CQVs had multiple sectors of adjacent or nearly-adjacent data, LP 12-502 (TIC 402980664;  $d=21$  pc,  $J=9.4$ ,  $T=11.1$ ) stood out due to the quality and content of its data. Figure 4 shows all available data from Sectors 18, 19, 25, 26, 53, 58, and 59, split into successive orbits; the star was observed at 120-second cadence whenever it was observable by TESS. We binned the light curve to 15-minute intervals for visual clarity, and required at least one (120-second cadence) flux measurement per bin. Points more than  $2.5\sigma$  above the median are drawn in gray, also for visual clarity. Missing data are not drawn. Figure 5 then shows the same data, but stacked into successive TESS orbits spanning half a lunar month each.

The average period, determined by measuring the PDM peak period over each sector independently, was  $\langle P \rangle = 18.5560$  hr. The range between the maximum and minimum sector-specific periods was measured to be about one minute. Based on this range, the star’s period is stable to at least one minute ( $\pm 0.017$  hr) over the three year baseline. However, in detail, a period shift of  $\pm 1$  minute would yield major phase drifts over the baseline; that time interval corresponds to roughly  $1/1000^{\text{th}}$  of a period, and we have observed 1500 cycles. The achievable period precision,  $\sigma_P$ , can be estimated as

$$\sigma_P = \frac{\sigma_\phi P}{N_{\text{baseline}}}, \quad (9)$$

for  $N_{\text{baseline}}$  the number of cycles in the observed baseline and  $\sigma_\phi$  the phase precision with which any one feature (e.g. a dip, or the overall shape of the sinusoidal envelope) can be tracked. Assuming  $\sigma_{\text{phi}} \approx 0.01$  yields an expected period precision  $\sigma_P \approx 0.45\text{sec} \approx 1.2 \times 10^{-4}$  hr. By visually fine-tuning over a grid in period, we eventually found  $P =$

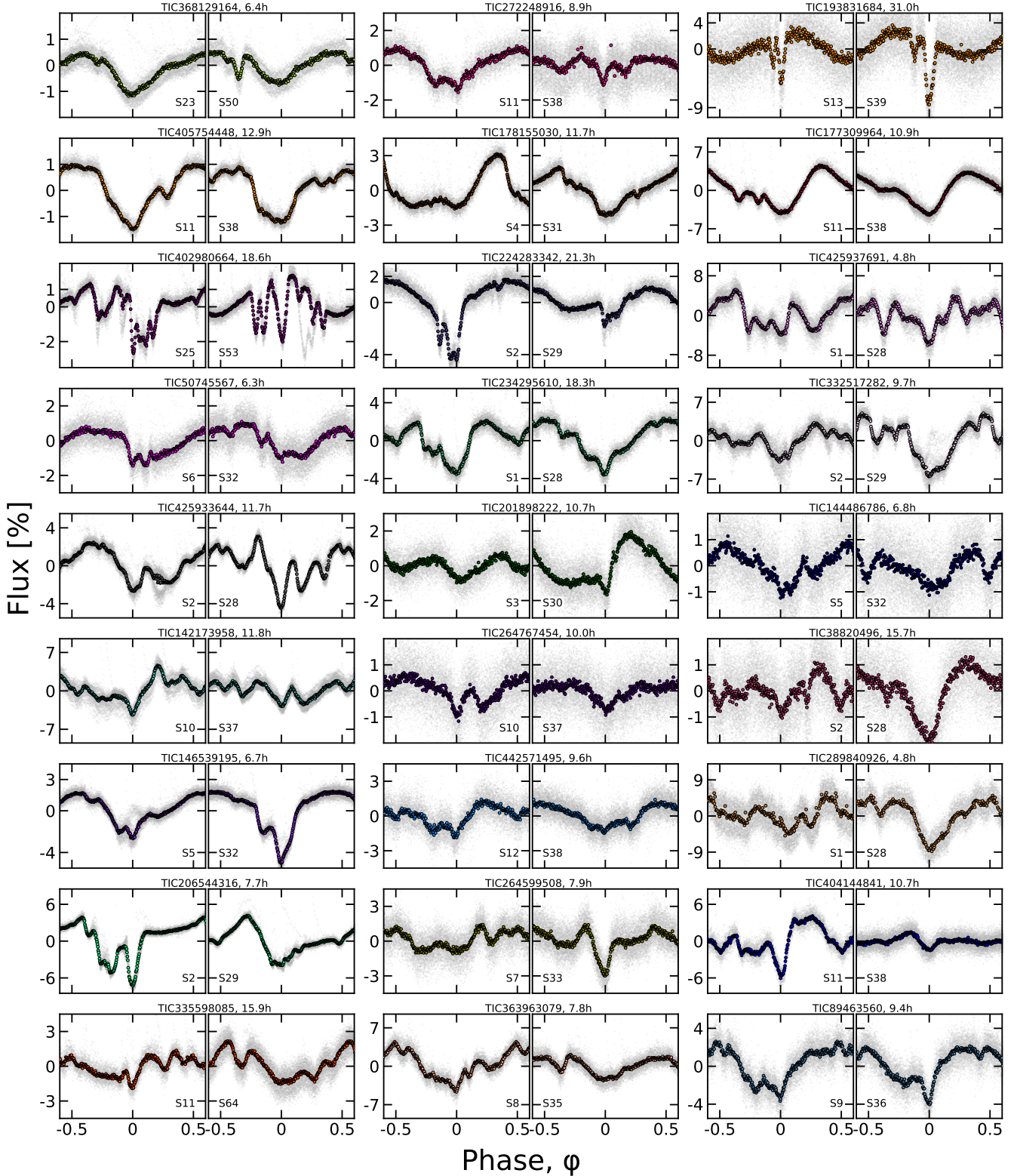


**Figure 3. CQVs keep their periods but change their shapes.** 32 of our 53 CQVs from Figure 2 had 120-second cadence TESS data available for a baseline of at least two years; the 27 brightest are shown here. Each panel shows one sector of TESS data, and is phased to its deepest minimum in flux. Each panel's title shows the TIC identifier and approximate period in hours. Text insets show the TESS sector numbers, which generally span two years, or at least 1,000 cycles. The vertical scale is fixed across sectors to clarify shape changes.

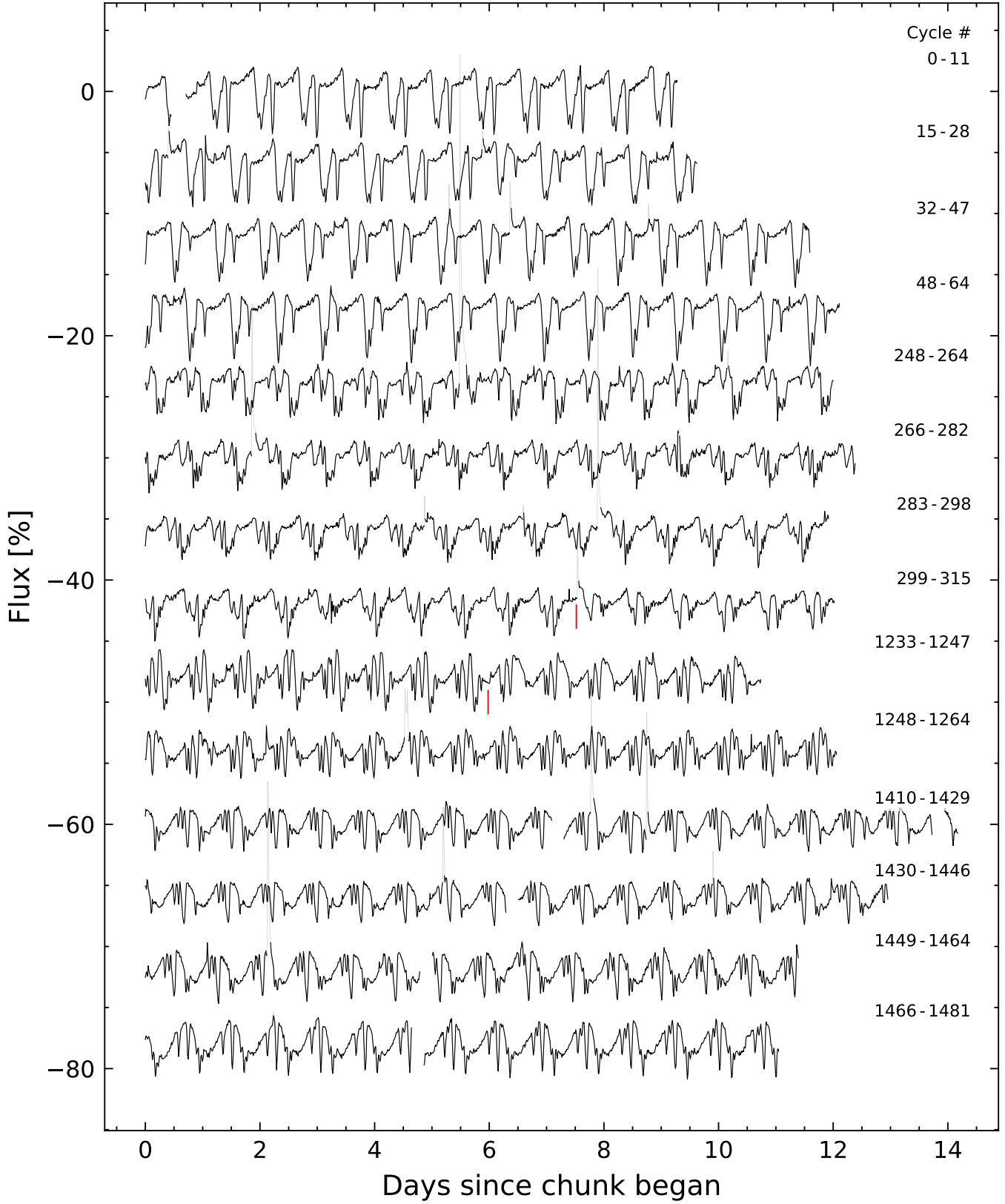


**Figure 4.** LP 12-502 (TIC 402980664) light curve, where each time chunk represents one TESS orbit. Data were acquired in Sectors 18-19, 25-26, 53, and 57-58. Flares are drawn in gray. The red vertical lines highlight apparently instantaneous state changes in the shape of the dip pattern. The light curve is binned to 15-minute intervals so that there are 96 points per day. Data gaps with more than one missing 15-minute cadence appear in white.

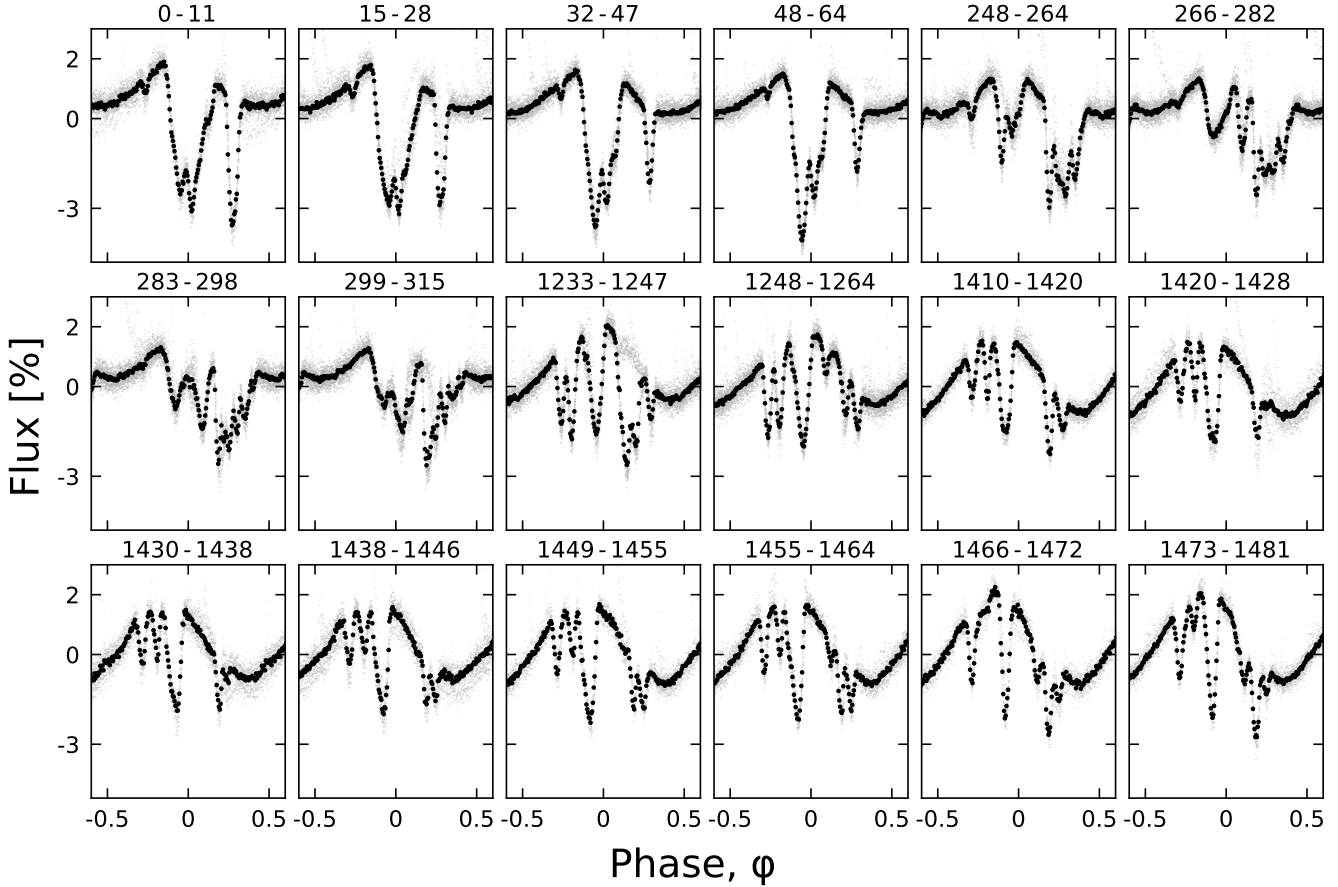


**Figure 5. Evolution of LP 12-502 ( $P=18.6$  h) at fixed period and epoch over three years.** Each panel shows one (stacked) TESS orbit; small text denotes relative cycle number. There are 200 binned black points per cycle. The TESS pointing law dictates time gaps; larger gaps tend to yield larger shape changes. The dips usually evolve over tens to hundreds of cycles. However cycles 1233-1264 show a dip that “switched” from a depth and duration of 3% and 3 hr to 0.3% and 1 hr over less than one cycle (cf. Figure 4).

$18.5611 \pm 0.0001$  hr, which seems to track certain features in the LP 12-502 light curve over its entire baseline.

What exactly is observed? For the first 64 cycles, the star shows a pattern reminiscent of an eclipsing binary, with four obvious local minima. We dub these dips  $\{1, 2, 3, 4\}$  at phases  $\{-0.28, -0.08, 0, 0.25\}$ , respectively. Over cycles 0 to 64, the depth of dips 1 and 3 remain roughly fixed. However dip 4 *decreases* in depth by about 2%, while dip 2 *increases* in depth, by about the same amount (see Figure 5). During cycles 48-64, it also seems that a fifth dip may be emerging, in the main “large” dip group.

There is then a 6-month (184 cycle) gap to Cycles 248-315, which show two intricately structured dip complexes, plus a small leading dip. The single leading dip is present at roughly the same phase as in cycles 0-64; they seem likely to be the same structure. Along a similar line of logic, it seems plausible that the first “dip complex” during cycles 248-264 represents an evolution of the initial complex seen during cycles 0-64, though with greatly reduced depth. During cycles 266-310, an additional local minimum develops between the

two complexes; this feature is best visualized on the river plots (Appendix B), and we discuss its (shorter) period below.

The second dip complex during cycles 248-315 shows the most substructure. During e.g. cycles 283-298, this single complex shows six local minima. The deepest dip is very sharp: it shows a flux excursion of 3.5% over about 22 minutes ( $0.02 P$ ), which is the steepest slope exhibited anywhere in this object’s remarkable dataset. After the sharp dip, there is a roughly exponential fall-off spanning about a quarter of a period, punctuated by coherent local minima and maxima which in detail (Appendix ??) have slightly longer periods than the sharp dip. The sharp leading dip only decreases during a sudden state-switch at BTJD 2030.7 (cycles 299-315), which happens immediately during a flare (Figure 4). The trailing dips remain afterwards.

Sectors 53–58 (cycles 1233-1481) are comparatively tame; they showed only four to six dips per cycle. Some dips remain stable in depth and duration over this five month interval. Other dips grow, like the one at  $\phi = +0.06$  between cy-

cles 1499 and 1481. Other dips, such as the one at  $\phi = +0.12$  in cycles 1233-1264, disappear entirely. The most dramatic state switch occurs during cycles 1233-1247, when a large dip “switches” from a depth of 3% and duration of 3 hours to a depth of 0.3%, and a duration of 1 hour.

#### 4.2.2. Lessons from LP 12-502

**STATE-SWITCHES REVEAL DIP INDEPENDENCE**—The state-switches seen in cycles 1233-1247 and 299-315 confirm that dips can disappear in less than one cycle, a point which has been previously appreciated (Stauffer et al. 2017). What is new in these particular changes, for instance cycles 1233-1264 of Figure 5, is that the morphology changes show that the dips can be *independent* and *additive*. In other words, throughout cycles 1233-1264, there are three local minima between phases of 0 and 0.3. They all have identical ingress times. The shape change during the transition implies that the leading dip that “turned off” (changed its depth), while the trailing two dips remained fixed in their depths. In other words, the structures producing these dips must be independent, to the degree that one can undergo a severe change, while the others can remain essentially identical. The state switches during cycles 248-264 and 299-315 share the same characteristic: it is always the *leading* dip of a complex that “switches off”, leaving the (fixed-depth) trailing dips in its wake.

**DIPS GROW MORE SLOWLY THAN THEY DISAPPEAR**—Although there are a few instances in which we observe dips “switch off” over less than one cycle, dip growth seems to happen more slowly. For instance, the dip that grows between phase 0 and 0.1 between cycles 260-290 begins to become visible around BTJD 1993.2, and grows in depth by about 2% over about six cycles, to become easily detectable by eye by BTJD 1997.7. The evolution of this particular dip is most clear in the river plots. The evolution of the latter dip group in cycles 1410-1481 is another example of this slow mode of dip growth.

**DIP DURATIONS**—The shortest timescale for any of the *individual* LP 12-502 dips seems to be  $\approx 0.06 P \approx 1.08$  hr. In comparison, using the stellar radius and mass derived in Section 2.3, the characteristic timescale  $T_{\text{dur}} \equiv R_* P / (\pi a)$  for the transit of a point-source at corotation is 1.03 hr (**uncertainties?**). This means that while some of the LP 12-502 dips are sufficiently long to require structures that are extended in orbital azimuth, the durations of other dips are consistent with effective radii for the occulting material  $R_{\text{eff}} \ll R_*$ . We also emphasize that this implies  $a/R_* \approx 5.8$  for this material, and so the analogous timescale at the stellar surface is about six times slower.

**DIP PERIODS**—Most of the LP 12-502 dips recur with a period of  $P = 18.5611 \pm 0.0001$  hr. However the river plots (Appendix B) reveal multiple distinct periodicities in the light curve for specific dips. For instance, in sectors 25-26, the local minimum that develops around cycle 262 has a period faster than the mean period by  $\approx 0.1\%$ , while some of the trailing local minima in the main dip complex have periods slower than the mean period, by  $\approx 0.04\%$ . In addition to the

fundamental period, we were able to identify at least four distinct periods shown by specific dips over the full Sectors 18-59 dataset, including periods at 18.5683, 18.5672, 18.5473, and 18.5145 hr, with a typical measurement uncertainty of  $\approx 0.0002$  hr. If each period corresponds to a dust clump, then this implies that multiple distinct clumps can orbit the star simultaneously, at marginally different separations.

## 5. DISCUSSION

### 5.1. Extremes

The closest CQV in our catalog is DG CVn (TIC 368129164;  $d=18$  pc), which is a likely member of AB Dor. To our knowledge, this manuscript is the first time that it has been noted as a CQV. The three brightest CQVs we have found are DG CVn ( $T=9.3$ ), TIC 405754448 ( $T=9.6$ ), and TIC 167664935 ( $T=10.3$ ).

The shortest period belongs to TIC 201789285, at 3.64 hr. The longest period belongs to TIC 405910546, at 37.9 hr. If that source turns out to be an eclipsing binary, then the next-longest would be TIC 193831684 (31.0 hr).

The lowest mass ( $\approx 0.12 M_\odot$ ) belongs to TIC 267953787. The catalog contains a few other stars with similar mass, which suggests the phenomenon may extend into the brown dwarf regime.

The most massive CQV in our sample is a subject of some interest because to date, the only stars reported to show the CQV phenomenon are M-dwarfs, with typical stellar masses  $\lesssim 0.3 M_\odot$  (Günther et al. 2022). TIC 405754448 and 405910546 however appear to have masses of 0.82 and  $0.60 M_\odot$  respectively. The next-highest masses are  $\approx 0.40 M_\odot$ . The masses for the former two objects are consistent with their CAMD locations, and their membership in LCC. Based on its light curve morphology, TIC 405910546 should be studied in greater depth, to confirm it is not an eclipsing binary. TIC 405754448 similarly shows distinct morphology from many of the CQVs in Figure 2, in that it has some of the lowest amplitude dips. However overall, both of these objects seem to suggest that the CQV phenomenon extends up in mass to pre-main-sequence K-dwarfs.

### 5.2. CQVs are quasiperiodic

A periodic signal repeats exactly; the CQVs do not, although their periods appear to be fixed to within measurement precision over thousands of cycles. They are therefore *quasiperiodic*. While this point has been suggested in studies by Günther et al. (2022) and Popinchalk et al. (2023), Figure 3 drives it home. This is a qualitative departure from the “persistent” vs. “transient” flux dip distinction described by Stauffer et al. (2017); while the dips can persist over timescales of even up to 100 cycles, all CQV dips seem to be transient over timescales of more than 1000 cycles (Figure 3).

With that said, one might expect a truly quasiperiodic process to be able to explore all phase angles with equal weight. LP 12-502, and many other CQVs, might have preferred phases. For LP 12-502, all of the dips happen over phases corresponding to only two thirds of the period. The other

third seems to be “out of limits” for any dipping material. This could be evidence either *a*) that some aspect the stellar magnetic field is strongly asymmetric, and can generate and hold extrinsic material at corotation, but only over two thirds of the equatorial circle, or *b*) that there is a material – for instance a disintegrating planetesimal swarm – that is distributed over an arc of the same angular extent ( $240^\circ$ ). We favor the former explanation, for reasons discussed below.

### 5.3. Dip asymmetries and dust geometries

The asymmetry of a dip can help diagnose the optical depth of the occulting material as a function of orbital phase angle. Sharp leading edges with trailing exponential egresses for instance have been previously seen for transiting exocomets and disintegrating rocky bodies (e.g. Rappaport et al. 2012; Brogi et al. 2012; Vanderburg et al. 2015; Zieba et al. 2019).

Examining Figure 2, it is not obvious whether the CQVs as a whole show any preference for sharper ingresses, or sharper egresses. In some cases (e.g. TIC 425933644), the continuum itself is not particularly well-defined, and so the meaning of “ingress” and “egress” are not particularly clear. In others, such as Sector 36 of TIC 89463560, there is a single clear sharp ingress with an exponential egress, which could be directly fit using e.g. a model analogous to those used for exocomets (e.g. Zieba et al. 2019). The main quantities of interest in such models would likely be the exponential decay time- and therefore length-scale, as well as the impact parameter and the inferred transit depth (and its implications for the equivalent “radius” of the transiting cloud). Although we briefly explored such models, it quickly became clear that careful modeling of sources such as LP 12-502 merits its own in-depth study. Connections could likely also be made to the toroidal geometries that are produced by outflowing atmospheres of transiting planets (e.g. McCann et al. 2019; MacLeod & Oklopčić 2022).

### 5.4. On the prominence scenario

In our view, the “prominence” scenario (Stauffer et al. 2017; Waugh & Jardine 2022), in which quiescent prominences analogous to those observed on the Sun become trapped in co-rotation may be the next-best contending model, after the idea of dust clumps doing the same thing. The prominence idea historically came from spectroscopic detections of transient Balmer- and resonance-line absorption seen for stars such as AB Dor and Speedy Mic (see e.g. Collier Cameron & Robinson 1989; Jeffries 1993; Jardine & Collier Cameron 2019). Neutral hydrogen clouds scatter chromospheric emission from the star, producing the observed spectroscopic line variations. The interpretation of those observations seems, in our view, secure.

The difference between the prominence and dust clump scenarios is essentially only in whether the occulting material of interest is neutral hydrogen, or dust. In the phrasing of the “frozen flux” condition of ideal rigid field magnetohydrodynamics, the tendency of both to become trapped at the corotation radius in the equatorial plane is tied to how of the four relevant forces (gravity, Lorentz, inertial Coriolis, and iner-

tial centrifugal), the Lorentz and Coriolis only act perpendicular to field lines, while gravity and the centrifugal force are in balance at  $R_{\text{cr}}$  (see Townsend & Owocki 2005, Sec. 2). The magnetic field strength is only relevant in this formulation of the system in that we must have  $R_{\text{sonic}} < R_{\text{cr}} < R_{\text{Alfvén}}$  in order for closed loops to exist that can support prominences (CITE Jardine/CollierCameron2019). In detail however, whether such magnetic fixed points lie in the equatorial plane, or elsewhere, depends on the star’s magnetic field geometry (Sanderson et al. 2023).

#### 5.4.1. Can gas absorption reproduce the observed chromaticity?

In our view, the strongest argument for why neutral hydrogen is ruled out as the occulting source is that we are seeing broadband flux variations that are deeper in the blue than in the red.

Based on our reading of Gray (1992, Ch. 8), it is somewhat challenging to get neutral hydrogen to have this type of chromaticity. Bound-bound absorption provides opacity only at narrow resonant lines. Bound-free absorption can provide wavelength-dependent opacity, but the absorption coefficients generally *grow* with increasing wavelength, rather than *shrink* as one needs in order to get deeper absorption in the blue than in the red. H<sup>-</sup> similarly fails as a viable opacity source for the same reason: its absorption coefficient peaks near 8500 Å, and is an order of magnitude smaller at  $\approx 3000$  Å (Gray 1992), following CITE Wishart 1979. Thompson scattering is also ruled out, because it is gray. Dust, with its relatively featureless but increasing extinction curve when going bluer into the optical, is to our knowledge the most obvious opacity source.

While the above line of reasoning seems fairly convincing, one flaw that we can point out in it is tied to  $\sigma$  Ori E. The logic presented above argues essentially that regardless of a star’s temperature, if relative depths of dips are seen to be deeper in the blue than in the red, then it is hard to get hydrogen to do it.  $\sigma$  Ori E shows dips that are deeper in the blue than in the red (Hesser et al. 1977), which have been understood in terms of absorbing circumstellar material (Townsend et al. 2005). This material however cannot be dust, due to the relevant sublimation timescales. It is instead thought to be sourced from bound-free absorption from neutral hydrogen (Townsend et al. 2005). Given these complexities, it clearly seems important for a future theoretical study to be conducted to determine to what degree the observed chromaticities match, or do not match, with expectations from radiative transfer. This issue has a key ability to resolve the question of whether the CQVs are caused by dust, or by gas.

#### 5.4.2. Does the timescale for CQVs to live inform the mechanism?

Independent of the theoretical basis for gas absorption, the prominence scenario may present another issue: why don’t stars in the Hyades and Praesepe show the phenomenon? in a broad sense, the prominence scenario argues that an intrinsic stellar process is key for generating the CQV phenomenon. If this were true, then stars of identical mass, size, and rotation periods might be expected to show the phenomenon

in equal number – irrespective of age. This is because the stellar dynamo is generated by fluid motions inside the star, which should be identical for stars of the same mass, size, and rotation period.

Between ages of  $\approx 100$  Myr (AB Dor, Pleiades, Psc-Eri) and  $\approx 700$  Myr (Praesepe and Hyades), a  $0.3 M_{\odot}$  star will shrink by  $\approx 10\%$ , from  $\approx 0.33 R_{\odot}$  to  $\approx 0.29 R_{\odot}$  (CITE MIST). This is not a particularly drastic size change. Similarly, many M-dwarfs have similarly rapid rotation periods at 700 Myr as they do at 100 Myr (CITE Rebull2022); the mean population does show some evidence for spin-down after the PMS contraction finishes, but a large fraction of the population is still spinning more rapidly than the  $\approx 2$  day limit at which the CQV phenomenon becomes less common.

Broadly speaking – the absence of old CQVs in our view seems to be more plausibly linked to a gradual depletion of dusty detritus from the planet formation era than it does to the changing stellar properties as stars gradually finish their pre-main-sequence evolution, and then continue to spin rapidly for many hundreds of millions of years.

The long-lived prominences inferred from the decades-old spectroscopic data, and dust-clouds inferred from K2+TESS, could of course also be pieces of a complementary picture.

### 5.5. Planets or planetesimal swarms near corotation?

Planet occurrence rate studies based on Kepler showed that around (early) M-dwarfs, there are  $\approx 0.1$  planets per star with sizes between  $1-4 R_{\oplus}$  and orbital periods within 3 days (Dressing & Charbonneau 2015). The number increases to  $\approx 0.7$  planets per star, for planets with  $1-4 R_{\oplus}$  and  $P < 10$  days. Extrapolating to *small* close-in planets, from say  $0.1-4 R_{\oplus}$  and within 10 days, it is reasonable to expect on average one planet per M-dwarf. TRAPPIST-1b ( $P=1.5$  days) is one example of this type of planet (CITE) orbits a  $0.08 M_{\odot}$  star.

Within the context of planet formation theory, the locations of these close-in planets are set by the location of the protoplanetary disk's magnetospheric truncation radius (see e.g. CITE for a review). In simple 1-D viscous accretion models, this truncation radius roughly coincides with the Keplerian corotation radius (CITE), though in detail factors of a few difference have been observed between the two (CITE IR studies). With models that have migrating compact multiplanet resonant chains, the inner-most planets arrive within  $\approx 5-10$  stellar radii within the first 100 Myr (e.g. CITE IZIDORO),

It is of course very tempting to attempt to interpret features of the CQV light curves in terms of the possible presence of close-in exoplanets, or even planetesimals. For instance, rocky planets this young would have molten global magma oceans analogous to those that existed on the Earth and Moon (e.g. CITE LICHTENBERG REVIEW), and thus would undergo significant outgassing and atmospheric escape. A scenario in which close-in rocky planets serve as a possible source of dust for the clouds is not entirely implausible, though it remains a subject of speculation.

Given the dip depth variations that are observed in systems like LP 12-502, one would be driven in this framework toward a picture of a disintegrating planetesimal swarm. The

dip-profile asymmetries during certain segments of the light curve plausibly match this idea; for instance, the complex in cycles 248-298 could be well-fit by a sharp leading edge that decays over  $0.2 P$  (3.7 hours). The earlier complex, during cycles 248-264 (pre-state-switch), could be fit by a similar profile. While the number of free parameters in this type of model is somewhat dizzying, we have no right to believe that nature need be simple.

Ultimately though, there are two glaring issues with the disintegrating planetesimal swarm idea. First, a large number of the dips show asymmetries in the *wrong direction* relative to the naive expectation of a trailing comet tail. Dust forward scattering might be one possible way out; so too might invoking non-exponentially decaying dust distributions as a function of azimuth. Second, and more serious, the (unseen) planets or planetesimals should be on *exactly periodic* orbits over observable timescales, on the presumption that the planetesimals would be massive enough to not feel any headwind or magnetic field. This is not what is observed. The fact that dips in sources such as LP 12-502 appear and disappear at *distinct phases* but with the same period seems to be a major challenge to tying the entire phenomenon to a single launching body. Similarly, the fact that the dips often respond to events like flares suggests that that the responsible material be much less massive than a 1–100- km sized planetesimal, and therefore more easily influenced by the stellar magnetic field.

### 5.6. From dippers to debris disks

The concordance model for planet formation invokes the presence of an accretion disk. The disk is truncated (by what?) at the magnetospheric truncation radius, which happens to often coincidentally be at the Keplerian corotation radius. In such a scenario, planetesimals and boulders can migrate inward due to Type X migration (CITE), until they hit a “dust trap” at the inner wall (CITE eg Kama2009, and related). Support for this model comes from the rotation periods of classical and weak-lined T Tauri stars (CITE Rebull2018,2019); from near-infrared interferometric observations that detect thermal emission from the disk wall (CITE CITE); and from the turn-over in the exoplanet orbital period distribution, which occurs around 5-10 days for FGK stars, and perhaps even closer-in for M-dwarfs (CITE Petitigura2022, and CITE for M-dwarfs).

Broadly, the existence of a dust trap at the disk truncation radius might be expected to trap larger boulders as well. Once the disk loses the gas, what happens to those boulders? They are no longer shielded. We then enter a phase of mass loss. Perhaps that phase is what we are observing.

## 6. CONCLUSIONS

In this work, we analyzed TESS 120-second cadence data collected between July 2018 and Sep 2022, and searched it for complex quasiperiodic variables (CQVs). Our search sample included 65760 K- and M-dwarfs within 150 pc, and is  $\gtrsim 80\%$  complete within 30 pc, and  $\lesssim 10\%$  complete at distances exceeding 100 pc.

In this sample of stars, we found 53 objects that showed complex quasiperiodic behavior over at least one observed TESS sector. These 53 bona fide CQVs are listed in Table ???. This table also includes an additional 17 candidate CQVs, whose designation is less certain. Analyzing the light curves of these objects, we draw the following conclusions.

- CQVs are *quasiperiodic*. While the mean periods in our sample seem to remain fixed over the span of available observations, the light curve shapes themselves evolve, similar to rotating stars.
- The same CQV can show dips with very similar but clearly distinct periods. LP 12-502, for instance, showed dips with four distinct periods within  $\pm 0.3\%$  of the fundamental period, sometimes simultaneous, and each lasting for up to 50 cycles.
- The CQV phenomenon persists for at least 150 Myr, based on the existence of CQVs in AB Dor, the Pleiades, and Psc-Eri. It may extend to even older ages, however the lack of detected CQVs in the Hyades and Praesepe suggest that the phenomenon is unique to the pre-main-sequence for M-dwarfs.
- CQVs evolve over timescales that are both secular ( $>100$  cycles) and impulsive ( $<1$  cycle). “State-switches” can cause dips to collapse instantaneously, and are often (but not exclusively) linked with observed optical flares. Dip growth however seems to happen over durations of at least ten cycles.
- The population-averaged duty cycle for CQVs seems to be  $\approx 75\%$ , based on the fraction of bona fide CQVs that “turned off” during TESS re-observations.

Many questions remain. After correcting for line-of-sight inclination, are most young M-dwarfs CQVs? What observational signatures distinguish the proposed models (Figure 1,

bottom row)? What organizational regularities characterize the CQV as a class of variable star? What physically sets the extremes of the CQV population, such as the longest rotation periods, hottest stellar temperatures, and oldest stellar ages? And finally, what connections, if any, do CQVs have to topics such as stellar evolution, M-dwarf magnetic fields, debris disks, and close-in exoplanets? While we have tried to point out possible connections, the most likely path toward definitive resolutions would be to observe a full phase curve of LP 12-502, or perhaps some other suitable object, using JWST/MIRI.

## ACKNOWLEDGMENTS

This work was supported by the Heising-Simons 51 Pegasi b Fellowship (LGB) TIC 402980664 was observed at 120-second cadence thanks to the TESS Guest Investigator programs G022252 (PI: J. Schlieder; Sectors 18, 19, 25, 26) and G04168 (PI: R. Jayaraman; Sector 53). **author contribution statement goes here** L.G.B. and R. J. conceived the project and executed the dip-based and Fourier-based searches, respectively. L.G.B. drafted the initial manuscript, and performed the cluster membership analysis. S. R. and R. J. vetted the results from the Fourier search. L.A.H. advised on project scope and experiment design. All authors assisted in manuscript revision.

**Software:** astrobase (Bhatti et al. 2021), lightkurve (Lightkurve Collaboration et al. 2018), scipy (Virtanen et al. 2020), TESS-point (Burke et al. 2020),

**Facilities:** Astrometry: Gaia (Gaia Collaboration et al. 2018,?). Imaging: Second Generation Digitized Sky Survey. Spectroscopy: Keck:I (HIRES; Vogt et al. 1994). Photometry: TESS (Ricker et al. 2015), Broadband photometry: 2MASS (CITE). APASS (CITE). Gaia (Gaia Collaboration et al. 2018,?). Pan-STARRS1 (CITE). SDSS (CITE). AllWISE (CITE).

## REFERENCES

- Allard, F., Homeier, D., & Freytag, B. 2012, Philosophical Transactions of the Royal Society A: Mathematical, Physical and Engineering Sciences, 370, 2765
- Ansdell, M., Gaidos, E., Rappaport, S. A., et al. 2016, ApJ, 816, 69
- Asplund, M., Grevesse, N., Sauval, A. J., & Scott, P. 2009, ARA&A, 47, 481
- Bailer-Jones, C. A. L., Rybizki, J., Fouesneau, M., Demleitner, M., & Andrae, R. 2021, AJ, 161, 147
- Barber, R. J., Tennyson, J., Harris, G. J., & Tolchenov, R. N. 2006, MNRAS, 368, 1087
- Basri, G. 2021, An Introduction to Stellar Magnetic Activity
- Bell, C. P. M., Mamajek, E. E., & Naylor, T. 2015, MNRAS, 454, 593
- Bhatti, W., Bouma, L., Joshua, et al. 2021, waqasbhatti/astrobase: astrobase v0.5.3, Zenodo
- Bodman, E. H. L., Quillen, A. C., Ansdell, M., et al. 2017, MNRAS, 470, 202
- Bouma, L. G., Winn, J. N., Ricker, G. R., et al. 2020, AJ, 160, 86
- Bouma, L. G., Curtis, J. L., Masuda, K., et al. 2022, AJ, 163, 121
- Boyle, A. W., & Bouma, L. G. 2023, AJ, 166, 14
- Bressan, A., Marigo, P., Girardi, L., et al. 2012, MNRAS, 427, 127
- Brogi, M., Keller, C. U., de Juan Ovelar, M., et al. 2012, A&A, 545, L5
- Burke, C. J., Levine, A., Fausnaugh, M., et al. 2020, TESS-Point: High precision TESS pointing tool, Astrophysics Source Code Library, record ascl:2003.001

- Cantat-Gaudin, T., Anders, F., Castro-Ginard, A., et al. 2020, *A&A*, 640, A1
- Capistrant, B. K., Soares-Furtado, M., Vanderburg, A., et al. 2022, *ApJS*, 263, 14
- Chen, Y., Girardi, L., Bressan, A., et al. 2014, *MNRAS*, 444, 2525
- Cody, A. M., Stauffer, J., Baglin, A., et al. 2014, *AJ*, 147, 82
- Collier Cameron, A., & Robinson, R. D. 1989, *MNRAS*, 238, 657
- Dahm, S. E. 2015, *ApJ*, 813, 108
- David, T. J., & Hillenbrand, L. A. 2015, *ApJ*, 804, 146
- Dressing, C. D., & Charbonneau, D. 2015, *ApJ*, 807, 45
- Fausnaugh, M., Morgan, E., Vanderspek, R., et al. 2021, *PASP*, 133, 095002
- Feiden, G. A. 2016, *A&A*, 593, A99
- Gagné, J., Mamajek, E. E., Malo, L., et al. 2018, *ApJ*, 856, 23
- Gaia Collaboration, Brown, A. G. A., Vallenari, A., et al. 2018, *A&A*, 616, A1
- Gray, D. F. 1992, The observation and analysis of stellar photospheres., Vol. 20
- Gully-Santiago, M. A., Herczeg, G. J., Czekala, I., et al. 2017, *ApJ*, 836, 200
- Günther, M. N., Berardo, D. A., Ducrot, E., et al. 2022, *AJ*, 163, 144
- Hesser, J. E., Ugarte, P. P., & Moreno, H. 1977, *ApJL*, 216, L31
- Hippke, M., David, T. J., Mulders, G. D., & Heller, R. 2019, *AJ*, 158, 143
- Jardine, M., & Collier Cameron, A. 2019, *MNRAS*, 482, 2853
- Jeffries, R. D. 1993, *MNRAS*, 262, 369
- Jenkins, J. M., Twicken, J. D., McCauliff, S., et al. 2016, in Society of Photo-Optical Instrumentation Engineers (SPIE) Conference Series, Vol. 9913, Software and Cyberinfrastructure for Astronomy IV, ed. G. Chiozzi & J. C. Guzman, 99133E
- Justesen, A. B., & Albrecht, S. 2021, *ApJ*, 912, 123
- Kerr, R. M. P., Rizzuto, A. C., Kraus, A. L., & Offner, S. S. R. 2021, *ApJ*, 917, 23
- Koen, C. 2021, *MNRAS*, 500, 1366
- . 2023, *MNRAS*, 518, 2921
- Lightkurve Collaboration, Cardoso, J. V. d. M., Hedges, C., et al. 2018, Lightkurve: Kepler and TESS time series analysis in Python, Astrophysics Source Code Library, record ascl:1812.013
- MacLeod, M., & Oklopčić, A. 2022, *ApJ*, 926, 226
- McCann, J., Murray-Clay, R. A., Kratter, K., & Krumholz, M. R. 2019, *ApJ*, 873, 89
- Meingast, S., Alves, J., & Rottensteiner, A. 2021, *A&A*, 645, A84
- Onitsuka, M., Fukui, A., Narita, N., et al. 2017, *PASJ*, 69, L2
- Palumbo, E. K., Montet, B. T., Feinstein, A. D., et al. 2022, *ApJ*, 925, 75
- Pecaut, M. J., & Mamajek, E. E. 2013, *ApJS*, 208, 9
- Popinchalk, M., Faherty, J. K., Curtis, J. L., et al. 2023, *ApJ*, 945, 114
- Rajpurohit, A. S., Reylé, C., Allard, F., et al. 2013, *A&A*, 556, A15
- Rappaport, S., Barclay, T., DeVore, J., et al. 2014, *ApJ*, 784, 40
- Rappaport, S., Levine, A., Chiang, E., et al. 2012, *ApJ*, 752, 1
- Ratzenböck, S., Meingast, S., Alves, J., Möller, T., & Bomze, I. 2020, *A&A*, 639, A64
- Rebull, L. M., Stauffer, J. R., Cody, A. M., et al. 2018, *AJ*, 155, 196
- Rebull, L. M., Stauffer, J. R., Bouvier, J., et al. 2016, *AJ*, 152, 114
- Ricker, G. R., Winn, J. N., Vanderspek, R., et al. 2015, *Journal of Astronomical Telescopes, Instruments, and Systems*, 1, 014003
- Robinson, C. E., Espaillat, C. C., & Owen, J. E. 2021, *ApJ*, 908, 16
- Rodriguez, D. R., van der Plas, G., Kastner, J. H., et al. 2015, *A&A*, 582, L5
- Sanderson, H., Jardine, M., Collier Cameron, A., Morin, J., & Donati, J. F. 2023, *MNRAS*, 518, 4734
- Somers, G., Cao, L., & Pinsonneault, M. H. 2020, *ApJ*, 891, 29
- Speagle, J. S. 2020, *MNRAS*, 493, 3132
- Stassun, K. G., Kratter, K. M., Scholz, A., & Dupuy, T. J. 2012, *ApJ*, 756, 47
- Stassun, K. G., Oelkers, R. J., Pepper, J., et al. 2018, *AJ*, 156, 102
- Stauffer, J., Collier Cameron, A., Jardine, M., et al. 2017, *AJ*, 153, 152
- Stauffer, J., Rebull, L., David, T. J., et al. 2018, *AJ*, 155, 63
- Stellingwerf, R. F. 1978, *ApJ*, 224, 953
- Tanimoto, Y., Yamashita, T., Ui, T., et al. 2020, *PASJ*, 72, 23
- Townsend, R. H. D., & Owocki, S. P. 2005, *MNRAS*, 357, 251
- Townsend, R. H. D., Owocki, S. P., & Groote, D. 2005, *ApJL*, 630, L81
- Vanderburg, A., Johnson, J. A., Rappaport, S., et al. 2015, *Nature*, 526, 546
- Vines, J. I., & Jenkins, J. S. 2022, *MNRAS*, 513, 2719
- Virtanen, P., Gommers, R., Oliphant, T. E., et al. 2020, *Nature Methods*, 17, 261
- Vogt, S. S., Allen, S. L., Bigelow, B. C., et al. 1994, in Society of Photo-Optical Instrumentation Engineers (SPIE) Conference Series, Vol. 2198, Instrumentation in Astronomy VIII, ed. D. L. Crawford & E. R. Craine, 362
- Waugh, R. F. P., & Jardine, M. M. 2022, *MNRAS*, 514, 5465
- Winn, J. N. 2010, in Exoplanets, ed. S. Seager, 55
- Zhan, Z., Günther, M. N., Rappaport, S., et al. 2019, *ApJ*, 876, 127
- Zieba, S., Zwintz, K., Kenworthy, M. A., & Kennedy, G. M. 2019, *A&A*, 625, L13
- Zuckerman, B. 2019, *ApJ*, 870, 27

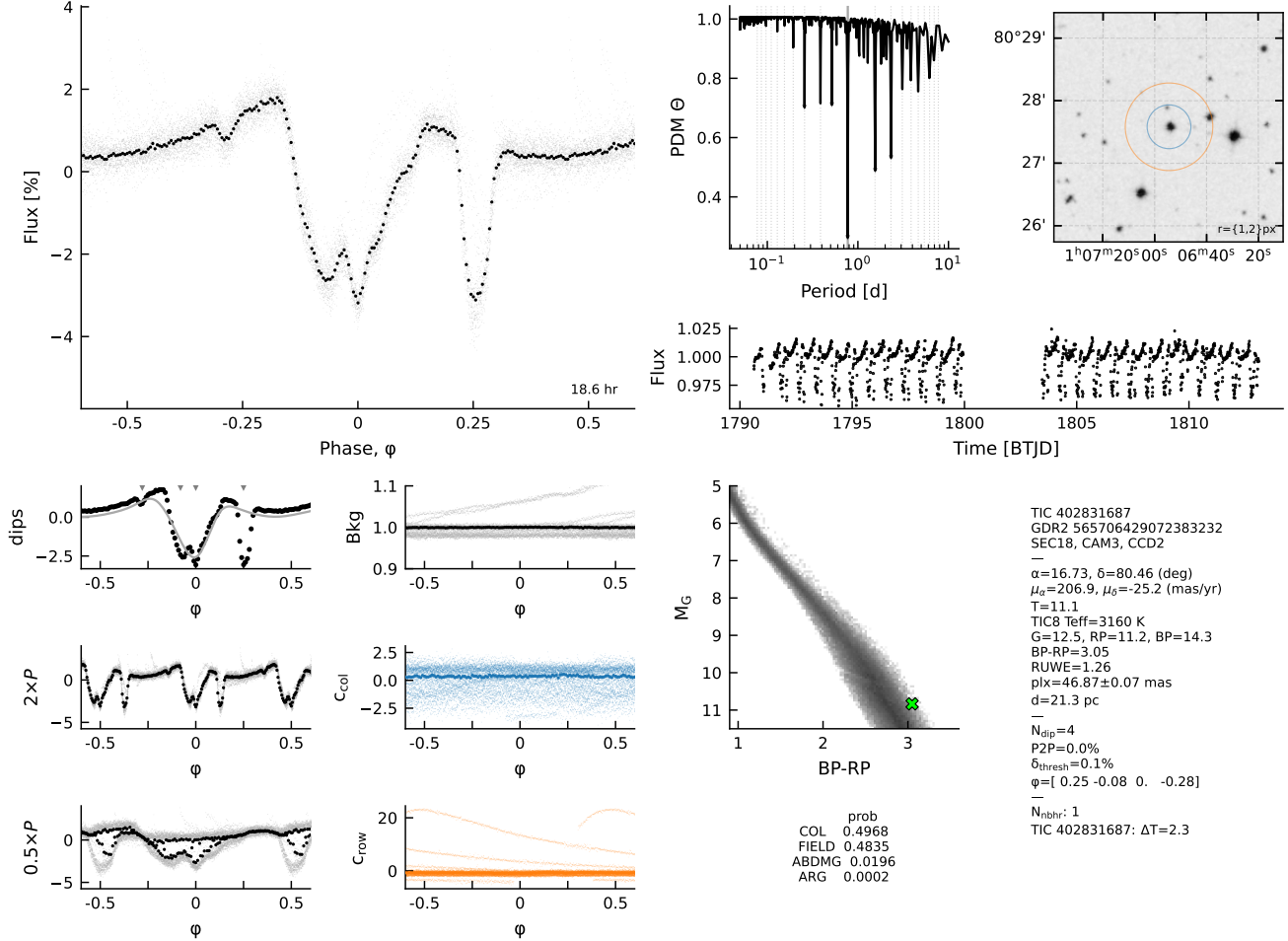


**Figure 6. Validation plots used to label CQVs.** The complete figure set, with one image per sector for each of 70 objects is available online **For internal collaboration review:** <https://www.dropbox.com/scl/fo/zlj3txot4cvymfb22wewu/h?dl=0&rlkey=3ec5f9o5xewrixzfkhkdenopa>. Panels are as follows. *a*): Phase-folded light curve; gray points are raw 2-minute data and black points are binned to 200 points per cycle. *b*): Phase-dispersion minimization (PDM) periodogram. Dotted lines show up to the 10<sup>th</sup> harmonic and subharmonic. *c*): DSS finder chart, with 1- and 2-TESS pixel radius circles displayed for scale. *d*): Cleaned light curve, binned to 20-minute cadence, in Barycentric TESS Julian Date (BTJD). *e*): Phase-folded light curve, binned to 100 points per cycle. The gray line denotes the automated spline-fit to the wrapped phase-folded light curve, and small gray triangles denote automatically identified local minima. *f*): Phase-folded light curve at twice the peak period. *g*): Phase-folded light curve at half the peak period. *h*): Phase-folded time-series within the “background” aperture defined in the SPOC light curves. *i*): Phase-folded flux-weighted centroid in the column direction. *j*): Phase-folded flux-weighted centroid in the row direction. *k*): Gaia DR2 color–absolute magnitude diagram. *l*): Information from Gaia DR2, TIC8, and the automated dip-counting search pipeline. “Neighbors”, abbreviated “nbhr”, are listed within apparent distances of 2 TESS pixels if  $\Delta T < 2.5$ . *m*): BANYAN- $\Sigma$  v1.2 association probabilities, calculated using positions, proper motions, and the parallax.

## APPENDIX

### A. VALIDATION PLOTS

Figure 6 shows the type of plot used to visually assess whether a source was likely to be a CQV, eclipsing binary, or simply a rapidly rotating star.

### B. LP 12-502

*The light curve*— Figure 7 shows another alternative view of Figure 5, but arranged to enable easy visual appreciation of transit timing changes, rather than transit depth changes. A best-fitting two-harmonic sinusoid has been independently fitted and subtracted from the Sector 18-19 data, 25-26 data, and 53, 58, and 59 data.

Finally, Figure 8 shows “river plots” of the same data, split into very similar intervals: the Sector 18-19 data, 25-26 data, 53 data, and 58-59 data. State changes are evident in these plots whenever there is a sudden change in color. **todo: fix missing data to be different from the flare color**

### C. NO ADDITIONAL POWER AT 20 SECOND CADENCE

Going from K2 to TESS, an important discovery was that the CQV shapes can significantly evolve, since the stars can vary over timescales of just a few minutes. We observed a set of CQVs between 2020 and 2021 using the TESS 20-second cadence mode (TESS DDT029). **todo: list the stars. todo: examine the 2min vs 20sec periodograms, and summarize in a few sentences whether any difference is there.**

### D. CHROMATICITY IN TIC 262400835

TIC 262400835 ( $d=174$  pc) is formally outside the scope of the current work. However, this CQV was observed using MuS-CAT2 on 2020 December 12, 13, and 16, and the results are pertinent enough to the present work. **todo: describe observations.**

We include **a table of the photometry** here to enable potential future deeper analyses of the chromaticity of this object class.

Generally, these data serve as a minor addition beyond the observations that have been acquired by [Onitsuka et al. \(e.g. 2017\)](#); [Tanimoto et al. \(e.g. 2020\)](#); [Günther et al. \(e.g. 2022\)](#); [Koen \(e.g. 2023\)](#) on this topic. [Koen \(2023\)](#) provides what we find to be the most lucid summary, and we quote: “amplitudes are almost always larger, the shorter the wavelength of the filter, but the relationship can be weak or non-monotonic.”

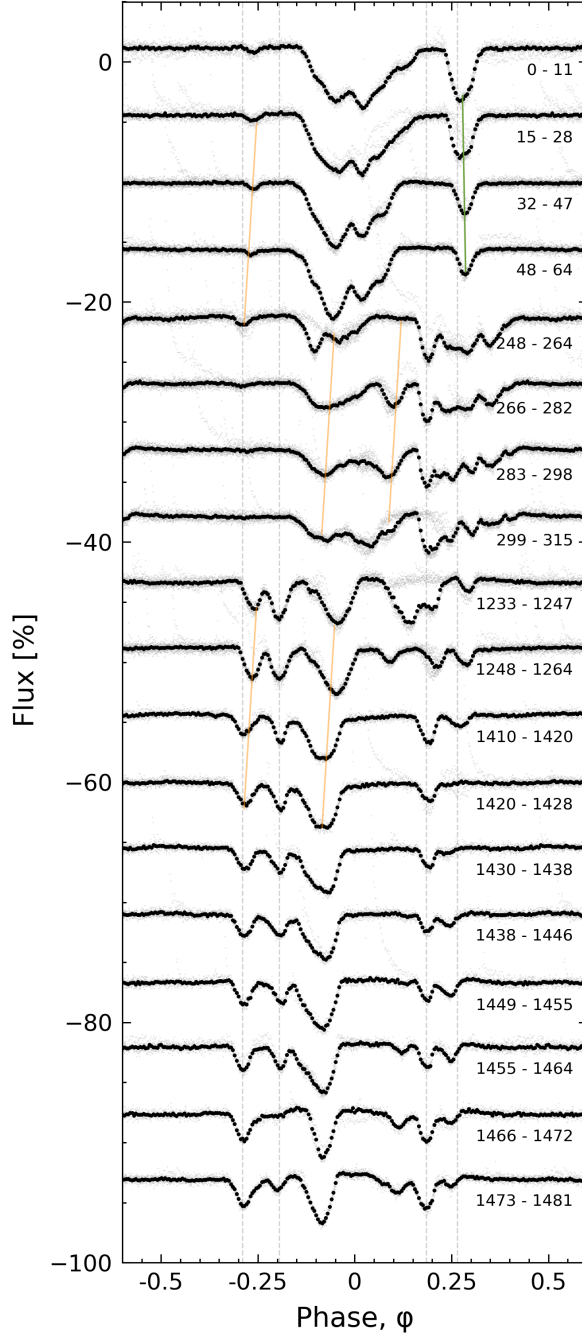


**Figure 7. Alternative view of the evolution of LP 12-502 (Figure 5), arranged to emphasize changes in transit times. There are 200 binned black points per cycle; a two-harmonic sinusoid has been subtracted over specific chunks in time (see text). Vertical gray lines are underplotted to help guide the eye to instances in which preferred dip phases synchronize over long baselines. The orange and green lines guide the eye to where dips appear to change the positions of their local minima.**

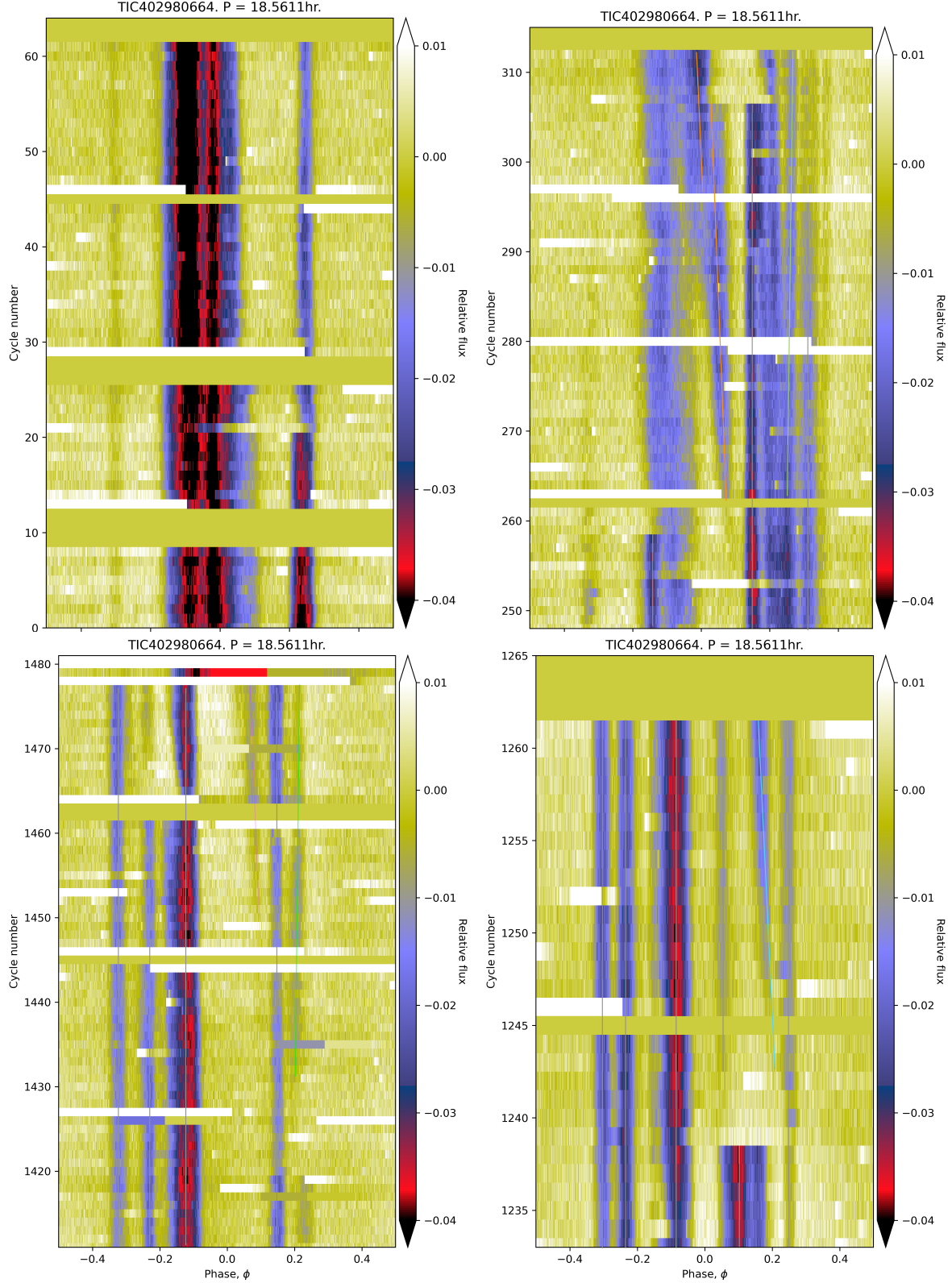


**Figure 8.** River plots of LP 12-502, showing (clockwise from top-left) Sectors 18-19, 25-26, 53, and 58-59. A two-harmonic sinusoid has been subtracted over specific chunks in time (see text). For Sectors 25-26 (cycles 248-315), three periods are overplotted:  $P=18.5611$  hr (gray vertical line); 18.5404 hr (orange); 18.5683 hr (green). For Sector 53, gray is identical, while cyan is 18.5145 hr. For Sectors 58-59, the magenta line is 18.5473 hr, and the green line is 18.5672 hr.

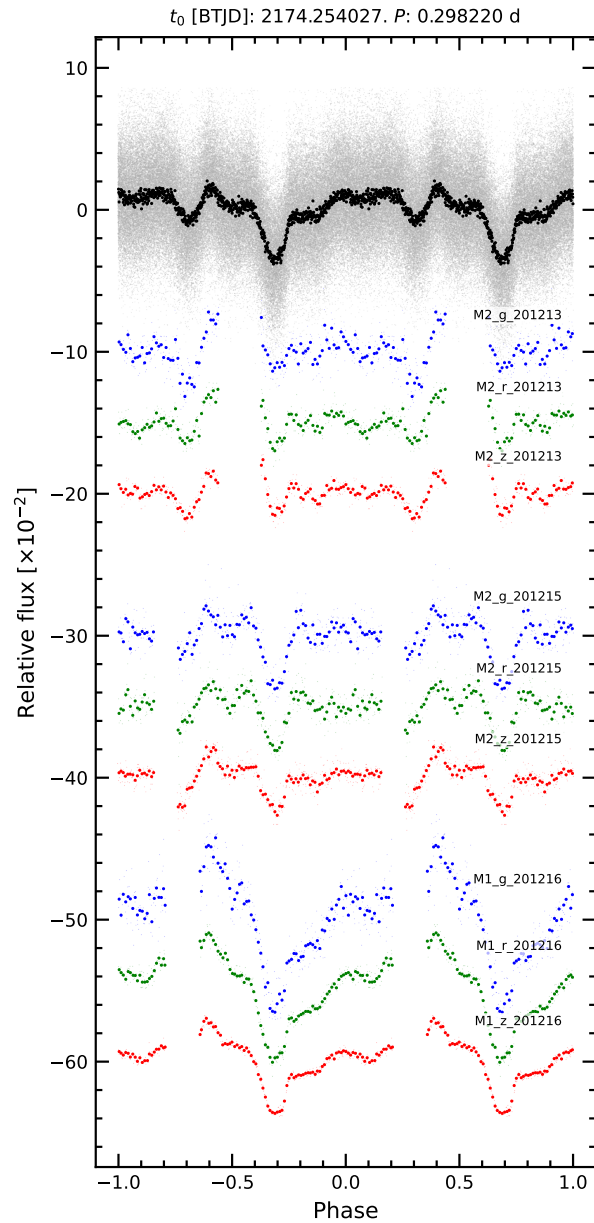


**Figure 9. Chromaticity in TIC 262400835.**